Highly Active and Robust Catalyst: Co₂B−Fe₂B Heterostructural Nanosheets with Abundant Defects for Hydrogen Production

Shuqing Zhou, Lianrui Cheng, Yi Liu, Jianniao Tian, Chenggong Niu, Wei Li,* Shoulei Xu,* Tayirjan Taylor Isimjan, and Xiulin Yang*

Read Online

ACCESS | 📊 Metrics & More | 📖 Article Recommendations | SI Supporting Information

ABSTRACT: A high-performance and reusable nonnoble metal catalyst for catalyzing sodium borohydride ($NaBH_4$) hydrolysis to generate H_2 is heralded as a nuclear material for the fast-growing hydrogen economy. Boron vacancy serves as a flexible defect site that can effectively regulate the catalytic hydrolysis performance. Herein, we construct a uniformly dispersed and boron vacancy-rich nonnoble metal Co_2B−Fe_2B catalyst via the hard template method. The optimized Co_2B−Fe_2B exhibits superior performance toward $NaBH_4$ hydrolysis, with a high hydrogen generation rate (5315.8 mL min^{-1} $g_{catalyst}^{-1}$), relatively low activation energy (35.4 kJ mol^{-1}), and remarkable cycling stability, outperforming the majority of reported catalysts. Studies have shown that electron transfer from Fe_2B to Co_2B, as well as abundant boron defects, can effectively modulate the charge carrier concentration of Co_2B−Fe_2B catalysts. Density functional theory calculations confirm that the outer electron cloud density of Co_2B is higher than that of Fe_2B, among which Co_2B with high electron cloud density can selectively adsorb BH_4^- ions, while the electron-deficient Fe_2B is favorable for capturing H_2O molecules, therefore synergistically promoting the catalytic $NaBH_4$ hydrolysis to produce H_2.
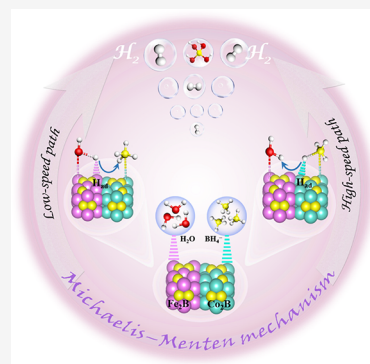
INTRODUCTION

The continued consumption of nonrenewable energy and resulting environmental pollution are urging people to accelerate the search for sustainable and clean energy.[1] Hydrogen (H_2) has stimulated substantial attention owing to its virtue of high heat of combustion (142 MJ kg^{-1}) and being environmentally friendly.[2] Nevertheless, the storage and transportation of hydrogen involve complex conditions, such as high pressure, which severely limits the rapid development of commercial hydrogen applications.[3] Therefore, it is necessary to develop safe and convenient hydrogen storage and production facilities to address the above-mentioned issues. According to current reports, common hydrogen storage materials are sodium borohydride ($NaBH_4$),[4,5] ammonia borohydride (NH_3BH_3),[6] magnesium hydride (MgH_2),[7] and lithium aluminum hydride ($LiAlH_4$).[8] Notably, these chemical hydrides have high hydrogen storage capabilities. They are expected to be the most potential candidates for providing pure hydrogen portable devices at room temperature, which fully align with commercial applications.[9] $NaBH_4$ has attracted significant attention due to its high hydrogen storage capacity (10.6 wt %), stability in alkaline solutions, mild reaction conditions, and nontoxicity.[10] Moreover, half of the hydrogen in $NaBH_4$ hydrolysis comes from water (eq 1), and this unique advantage makes it a promising method for hydrogen production. The ideal hydrolysis reaction equation of $NaBH_4$ is as follows[11]:

$$NaBH_4 + (2 + x)H_2O \xrightarrow{Catalyst} NaBO_2 \cdot xH_2O + 4H_2 \quad (1)$$
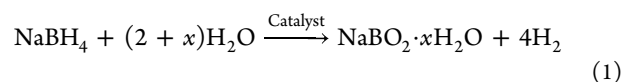
Although $NaBH_4$ is a promising hydrogen storage material, its use can be expensive and often generates significant waste. Surprisingly, researchers found that using ball milling to regenerate $NaBH_4$ from byproducts allowed the use of low-cost materials, reduced waste generation, and improved reaction kinetics. However, the process can be challenging and requires careful optimization of the reaction conditions, such as the milling time, ball-to-powder ratio, and hydrogen pressure.[12] Furthermore, the slow self-hydrolysis of $NaBH_4$ exhibits sluggish kinetics, which hinders the rapid industrialization process. Therefore, it is necessary to introduce an effective catalyst for rapid hydrogen supply.[13]
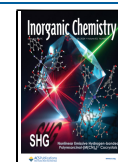
Currently, due to the expensive price of precious metal, nonprecious metal catalysts have become a research hotspot. Extensive literature has revealed that amorphous metal−B alloys are recognized as ideal candidates for $NaBH_4$ hydrolysis catalysts due to their exciting activity and cheap price.

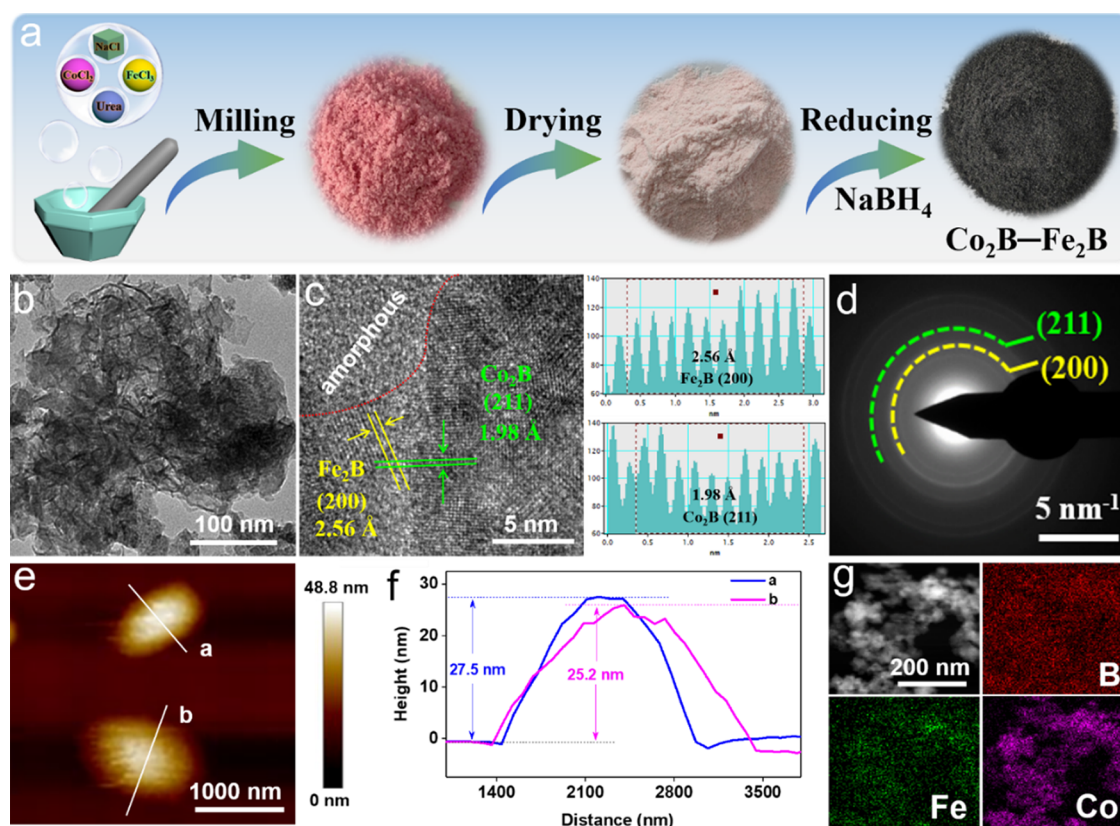**Figure 1.** (a) Schematic diagram of the synthesis of Co_2B-Fe_2B. (b) TEM image, (c) HR-TEM image, (d) SAED image, (e, f) AFM image and the corresponding height profile, and (g) HAADF-STEM image and elemental mappings (B, Co, and Fe) of Co_2B-Fe_2B.

Examples include amorphous $Cr-Co-B$,[14] spiral microalgae-like $Co-B$,[15] and $Co-Ni-B$ nanocrystals.[16] Nevertheless, the exothermic nature of the boride preparation reaction leads to a high degree of agglomeration for these materials, which limits its application in hydrogen production reactors. To better disperse the catalyst, the contact area between the catalyst and reactants can be increased by using easily dispersible templates or high specific surface area carrier materials.[17] Sodium chloride templates are excellent candidates for the preparation of three-dimensional materials, not only are the raw materials abundant, but the templates can be removed with a simple water wash.[18] For instance, Zeng et al. prepared three-dimensional thin-film nanomaterials with unique morphology using the sodium chloride template method, which increased the dispersion of catalysts and improved the catalytic performance.[19] Moreover, massive studies have proposed that an enriched defect can effectively modify the surface microstructure, electronic structure, and carrier concentration of a catalyst, thereby enhancing its catalytic activity.[20] In our previous work, we demonstrated that phosphorus and oxygen vacancy engineers could regulate the catalysts to exhibit superior catalytic activity in generating hydrogen through $NaBH_4$ hydrolysis.[21,22]

In this study, we used the NaCl template and vacancy engineering strategies to fabricate Co_2B-Fe_2B composites with abundant boron vacancies and uniform dispersion. The crystal structure, surface morphology, and electronic state of Co_2B-Fe_2B were analyzed through various characterization techniques, including X-ray diffraction (XRD), scanning electron microscopy (SEM), X-ray photoelectron spectroscopy (XPS), and electron paramagnetic resonance (EPR). We conducted

performance testing on the H_2 generation of $NaBH_4$ hydrolysis, where the optimized Co_2B-Fe_2B exhibited the highest H_2 generation rate (HGR = 5315.8 mL min^{-1} $g_{catalyst}^{-1}$) with an activation energy of 35.4 kJ mol^{-1} and excellent reusability. This exceptional performance was attributed to the electronic synergy between the components of Co_2B-Fe_2B and the boron vacancies. In addition, density functional theory (DFT) calculations revealed that Co_2B-Fe_2B had the lowest transition state energy barrier ($\Delta G_4 = 1.18$ eV) in the rate-determining step compared with Co_2B ($\Delta G_4 = 1.68$ eV) and Fe_2B ($\Delta G_4 = 1.90$ eV), supporting faster reaction kinetics. Overall, our findings demonstrate the promising potential of Co_2B-Fe_2B composites with abundant boron vacancies and uniform dispersion for efficient H_2 generation through $NaBH_4$ hydrolysis.

RESULTS AND DISCUSSION

Synthesis Strategy and Microstructure Analysis. As shown in Figure 1a, we synthesized boron vacancy-rich Co_2B-Fe_2B by employing the NaCl rigid template strategy. To achieve this, we added $CoCl_2 \cdot 6H_2O$, NaCl, $CO(NH_2)_2$, and $FeCl_3 \cdot 6H_2O$ to a mortar in the appropriate proportions and thoroughly milled the mixture at room temperature. The resulting sample was then dried in an oven. Next, we ground the dried sample again and added $NaBH_4$, mixing it thoroughly. Finally, we washed the Co_2B-Fe_2B with deionized water to remove NaCl and collected it by centrifugation.

The morphology of Co_2B-Fe_2B was examined by SEM and transmission electron microscopy (TEM). The obtained Co_2B-Fe_2B displayed a porous particulate structure formed by stacking sheet-like components, as depicted in Figure S1a.

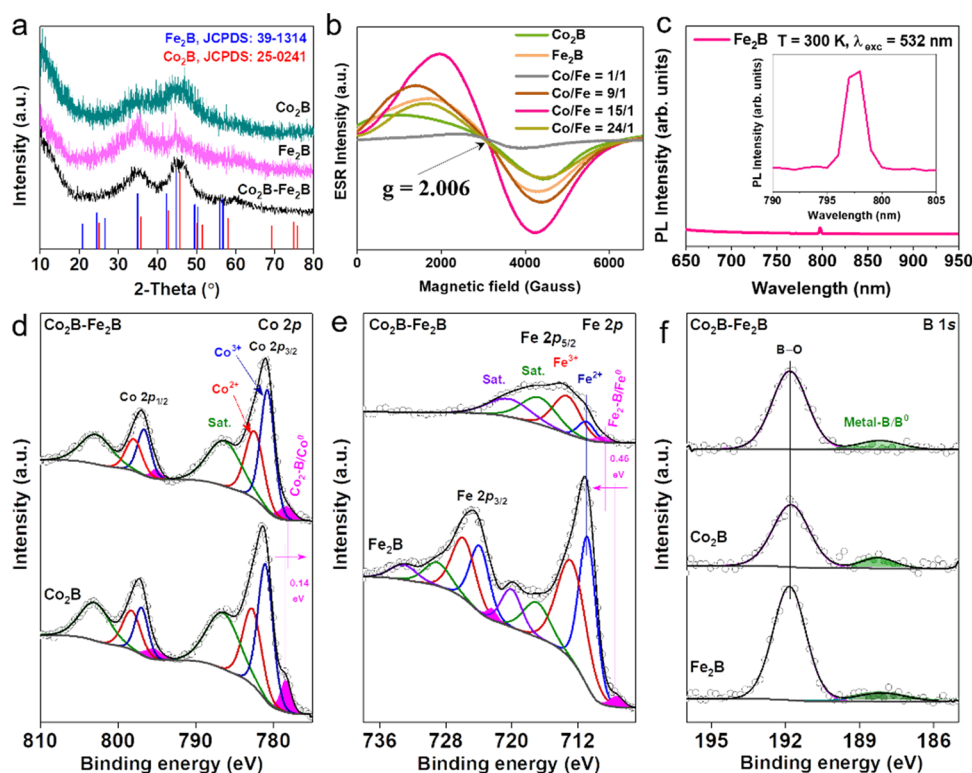**Figure 2.** (a) XRD patterns of Co_2B, Fe_2B, and Co_2B-Fe_2B. (b) EPR spectra of the catalysts. (c) Room temperature μ-PL spectra measured under λ = 532 nm excitation for Fe_2B. The inset shows an enlarged scale PL band around λ = 797 nm in the enlarged scale. High-resolution XPS of (d) Co 2p, (e) Fe 2p, and (f) B 1s regions of Co_2B, Fe_2B, and Co_2B-Fe_2B.

In contrast, the Co_2B-Fe_2B catalyst prepared without the NaCl template exhibited irregular particle agglomeration (Figure S1b), indicating that the NaCl template strategy effectively builds sheet-like structural components and inhibits aggregation. TEM analysis of Co_2B-Fe_2B revealed a translucent film structure with abundant folded edges, as shown in Figure 1b. The high-resolution TEM (HR-TEM) image (Figure 1c) confirmed the presence of Co_2B and Fe_2B phases, with lattice fringe of approximately 1.98 and 2.56 Å corresponding to Co_2B (211) and Fe_2B (200) crystal planes, respectively.[23,24] A distinct amorphous interface was observed between the two crystalline phase components, which has been shown in previous studies to expose more active sites at the interface between crystalline and amorphous states.[25] Selected area electron diffraction (SAED) identified the diffraction spots of Fe_2B (200) and Co_2B (211), further confirming the successful synthesis of the Co_2B-Fe_2B composite (Figure 1d). Atomic force microscopy (AFM) analysis (Figure 1e,f) further confirmed that the thickness of the Co_2B-Fe_2B nanosheets is about 26.4 nm. The high-angle annular dark-field scanning TEM (HAADF-STEM) and corresponding elemental mapping (Figure 1g) indicated a uniform distribution of B, Fe, and Co elements throughout the architecture.

Crystallinity and Defect Analysis. The XRD patterns were used to characterize the crystalline properties of the synthesized samples. The coexistence of Co_2B (JCPDS: 25-0241) and Fe_2B phase (JCPDS: 39-1314) was detected, as shown in Figure 2a, indicating the successful formation of Co_2B-Fe_2B.[26,27] For comparison, single Co_2B and Fe_2B were prepared without any crystalline impurities. EPR measurements were performed to characterize the vacancies (Figure 2b). The Co_2B, Fe_2B, and Co_2B-Fe_2B exhibited clear

symmetric signals at g = 2.006, indicating the presence of the same defect in the material structure, which is consistent with the electron trapping at B vacancies.[28,29] Compared with Co_2B and Fe_2B, Co_2B-Fe_2B showed the strongest EPR signal, implying more defects. Moreover, due to the presence of numerous spin peaks in the Co element, we opted for the Fe_2B catalyst for concentration spectroscopy testing, as it remains unaffected by spin peaks from other elements. The observed broad near-infrared PL spectral band around λ = 797 nm aligns with the light absorption band of B vacancies, providing additional confirmation of their existence.[30,31] The increase in defects can change the carrier concentration of the catalyst and enhance the synergistic effect between the components, resulting in better catalytic performance.[32]

XPS Analysis. XPS was used to analyze the surface chemical state and electron structure of the samples. The XPS survey spectrum of Co_2B-Fe_2B confirmed the presence of Co, Fe, and B elements (Figure S2). High-resolution XPS spectra of C 1s regions were analyzed using C–C (284.8 eV), C–O (286.0 eV), and C=O (288.7 eV) as calibration criteria (Figure S3).[33,34] The high-resolution Co $2p_{3/2}$ spectrum of Co_2B-Fe_2B was split into four peaks, corresponding to Co^0/Co_2–B (778.4 eV), Co^{3+} (780.8 eV), Co^{2+} (782.5 eV), and a satellite peak (786.3 eV) (Figure 2d).[23,35,36] Amorphous metal borides oxidize spontaneously when exposed to air, forming surface oxides and, therefore, multivalent cobalt.[37,38] Notably, the typical Co^0/Co_2–B in Co_2B-Fe_2B showed a negative shift of 0.14 eV compared to Co_2B, indicating a strong electronic interaction between the components. The high-resolution Fe 2p XPS spectra of Co_2B-Fe_2B were fitted into five peaks, which were assigned to Fe^0/Fe_2–B (708.9 eV), Fe^{2+} (710.9 eV), Fe^{3+} (713.3 eV), and two satellite peaks (Figure 2e).[24,39]
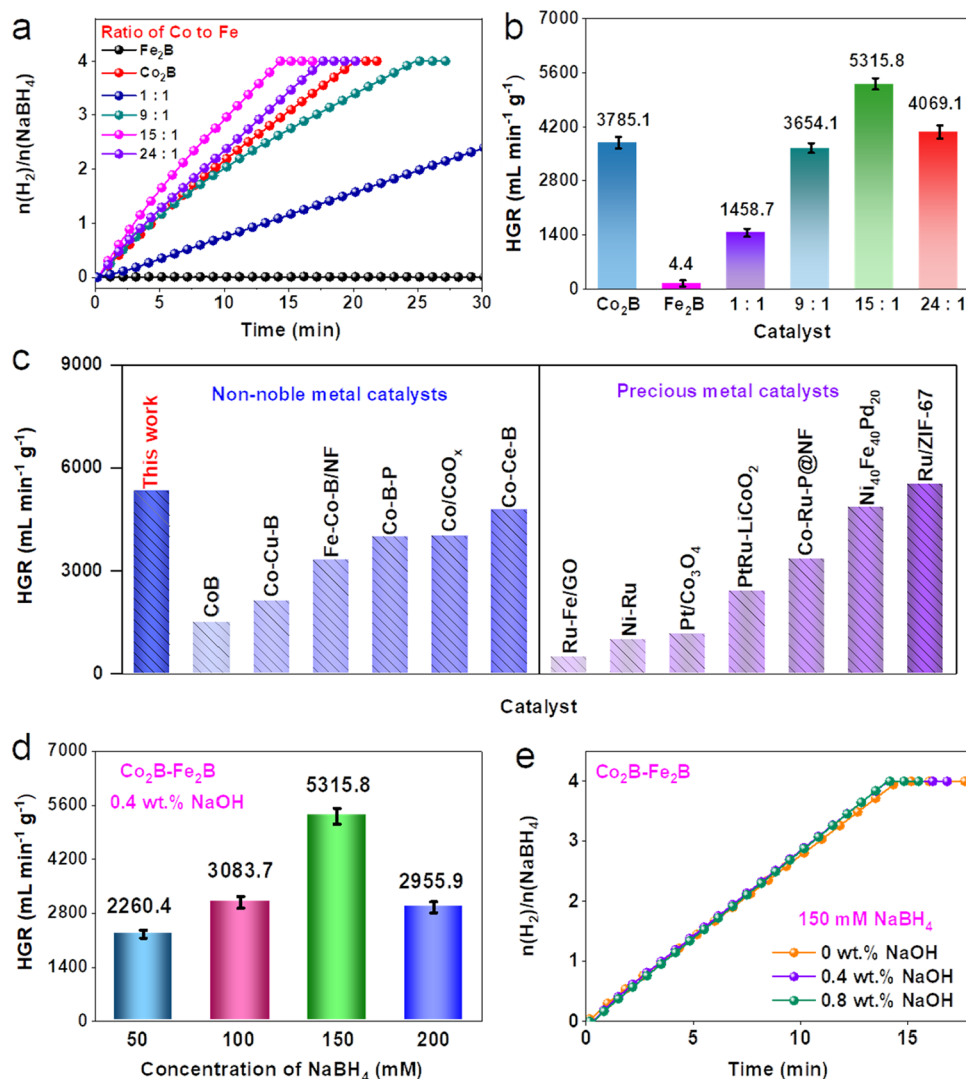
Figure 3. (a) Influence of different catalysts on $NaBH_4$ hydrolysis to produce hydrogen and (b) corresponding HGR value of the catalyst from (a). (c) Comparison of HGR values for different catalysts (Table S3). (d) Effect of different $NaBH_4$ contents on HGR of Co_2B-Fe_2B at the same NaOH concentration (0.4 wt %). (e) Effect of different NaOH contents on HGR of Co_2B-Fe_2B at the same $NaBH_4$ concentration (150 mM). All tests were performed at 298 K.

In contrast, the binding energies of Fe^0/Fe_2-B were positively shifted by 0.46 eV compared to Fe_2B. The change in binding energy between Co 2p and Fe 2p implies a strong electronic interaction between Co_2B and Fe_2B components.[40] The strong electronic interaction between components can effectively reduce the reaction energy barrier of the Co_2B-Fe_2B catalyst, thereby increasing the catalytic reaction rate. The B 1s core-level XPS spectra of Co_2B, Fe_2B, and Co_2B-Fe_2B were deconvoluted into two peaks of metal−B/B^0 and B−O bonds, revealing the existence of a metal−B alloy (Figure 2f).[41] Moreover, the different binding energies of metal−B/B^0 bonds among Co_2B, Fe_2B, and Co_2B-Fe_2B further revealed a strong synergistic effect between the components after alloying.[42,43]

Catalytic Hydrolysis Performance Analysis. The catalytic performance was evaluated in an alkaline $NaBH_4$ solution at 25 °C, and the hydrolysis setup is illustrated in Figure S4. Experimentally, a single $NaBH_4$ solution undergoes slow self-hydrolysis at room temperature and is unstable (Figure S5). However, the self-hydrolysis slowed significantly when $NaBH_4$ was dissolved under alkaline conditions, suggesting that $NaBH_4$ was stable in an alkaline solution

(Figure S6). Initially, we investigated the effect of Co/Fe ratios on the catalytic performance of Co_2B-Fe_2B catalysts on H_2 production. As shown in Figure 3a, the H_2 production rate increased until the molar ratio reached 15/1 and then decreased as the Co content continued to increase. The actual metal content of the catalysts was determined by ICP-AES tests (Table S2). Co_2B-Fe_2B exhibited the highest activity with an HGR of 5315.8 mL min^{-1} $g_{catalyst}^{-1}$ at a molar ratio of Co/Fe of 15:1, outperforming Co_2B, Fe_2B (Figure 3b), and Co_2B-Fe_2B-Without-NaCl (Figure S7). Despite high metal content, nonprecious metal catalysts, such as Fe_2B-Co_2B, show low TOF values (21.1 mol_{H2} min^{-1} mol_{metal}^{-1}), prompting the use of HGR values in the literature.[17] The excellent $NaBH_4$ hydrolysis ability of the Co_2B-Fe_2B catalyst can be attributed to the abundance of boron vacancies, which enhanced the charge carrier concentration of the catalysts as well as promoted the electronic synergism between the Co_2B and Fe_2B components.[44] Moreover, the remarkable HGR of the Co_2B-Fe_2B catalyst outperformed most of the documented nonnoble and noble metal catalysts (Figure 3c).
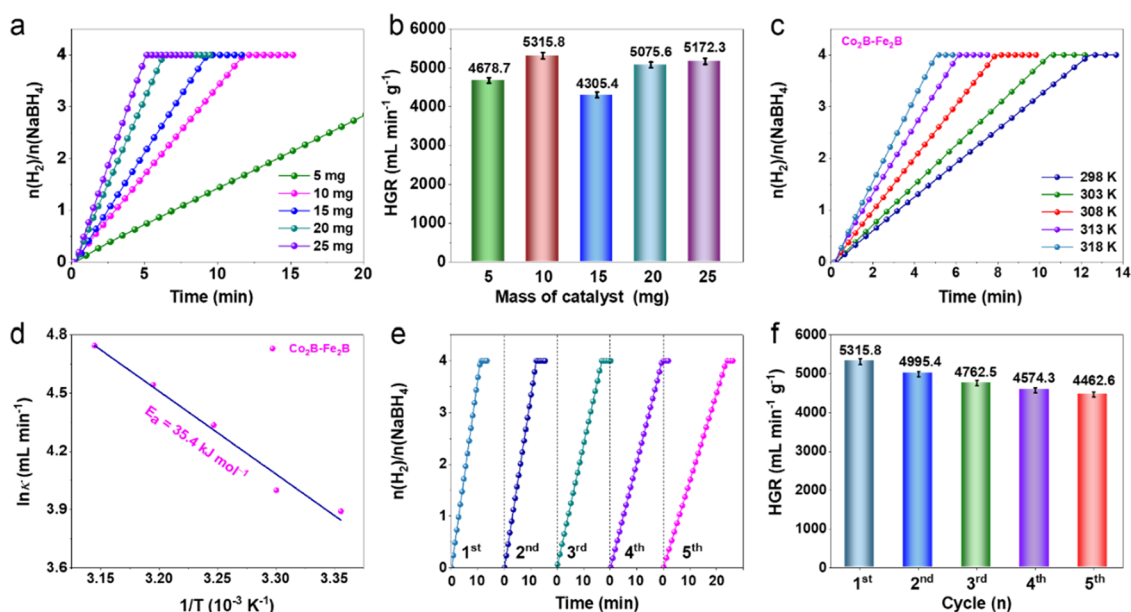
Figure 4. (a) Relationship between the H_2 generation rates and reaction time for different masses of catalysts. (b) Summarized HGR values from (a). (c) Relationship between the H_2 generation rates and reaction time of different reaction temperatures (298–303 K). (d) Summarized Arrhenius diagram from (c). (e) Reusability test of the Co_2B–Fe_2B catalyst at 25 °C. (f) Summarized HGR values from (e). All the tests were performed in 150 mM $NaBH_4$ + 0.4 wt % NaOH solution.
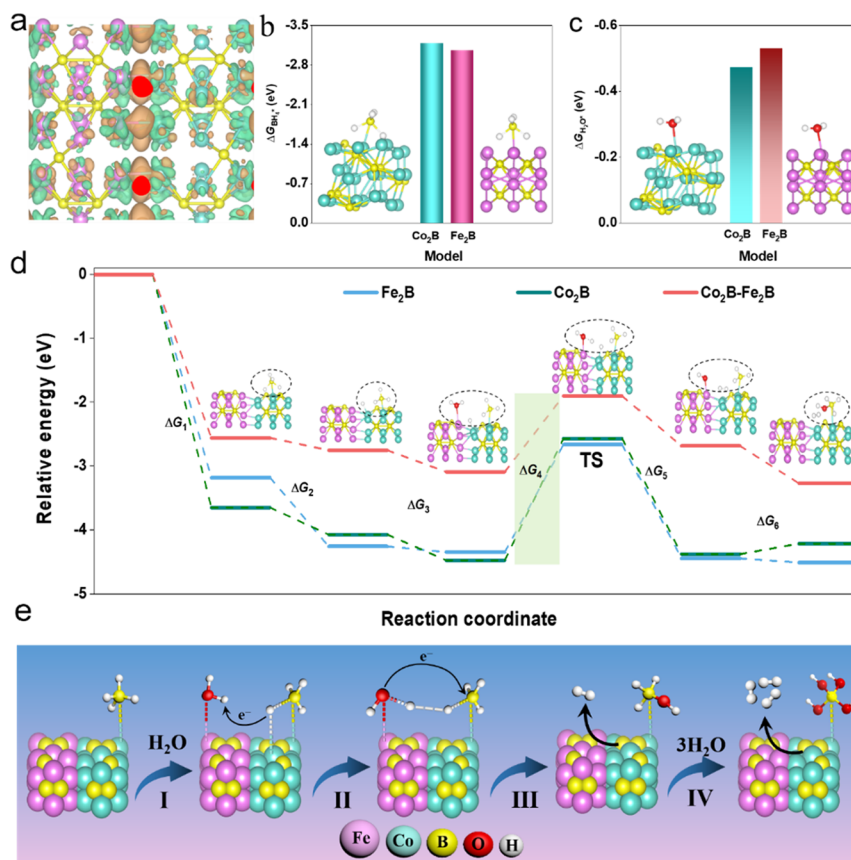

Figure 5. (a) Charge-density distribution of the Co_2B–Fe_2B model. The pink, cyan, and yellow balls represent the Fe, Co, and B atoms, respectively. (b) Gibbs free energy profiles for the BH_4^- adsorption (ΔG_{BH4*}), and the inset shows the optimized BH_4^- adsorption configuration on the Co_2B and Fe_2B sites. (c) Gibbs free energy profiles for H_2O adsorption (ΔG_{H2O*}), and the inset shows the optimized H_2O adsorption configuration on the Co_2B and Fe_2B sites. (d) Free energy curves of Co_2B, Fe_2B, and Co_2B–Fe_2B for the hydrolysis of $NaBH_4$. (e) Proposed mechanism diagram of $NaBH_4$ hydrolysis for H_2 generation.

The effect of different $NaBH_4$ concentrations on catalytic performance was investigated using 10 mg of Co_2B-Fe_2B catalyst with the same NaOH concentration. As depicted in Figure 3d, the HGR increased progressively with an increase in the $NaBH_4$ concentration up to 150 mM, beyond which the HGR value rapidly declined. The reason for this result was the low concentration of BH_4^- relative to that of H_2O, which restricted the supply of reactants to the Co_2B-Fe_2B catalyst surface, thus limiting the reaction. By contrast, higher $NaBH_4$ concentrations (200 mM) increased the viscosity of the solution, which limited the rate of mass transfer and ultimately led to an inhibitory effect on the catalytic rate.[45] Examining various reports, we found that the type of catalyst plays a crucial role in the outcome of the hydrolysis of $NaBH_4$.[45,46]

Furthermore, by controlling the pH of the solution, the self-hydrolysis of $NaBH_4$ in water can be inhibited. Therefore, the effect of NaOH concentration on the hydrolysis reaction was examined. As shown in Figure 3e, the nearly constant HGR observed at different NaOH concentrations suggests that NaOH concentration has a zero-order kinetics response.[14] The results suggest that the role of NaOH is merely to provide an alkaline environment to inhibit the self-hydrolysis of $NaBH_4$.[22]

In addition, it is essential to discuss the impact of catalyst concentration on $NaBH_4$ hydrolysis. As shown in Figure 4a, the time required to produce the same volume of hydrogen decreased with an increasing amount of catalyst, indicating the presence of more active sites.[47] However, after normalization of the HGR, it was found that the optimal amount of catalyst was 10 mg, indicating that the active sites were utilized most effectively under this condition (Figure 4b). The effect of temperature on catalyzing H_2 generation for Co_2B-Fe_2B was investigated within the range of 298−318 K. As shown in Figure 4c, there was an increase in HGR with an increase in the reaction temperature. The calculated activation energy of Co_2B-Fe_2B was 35.4 kJ mol^{-1}, based on the Arrhenius equation (Figure 4d). This value was lower than most recently reported catalysts (Table S3), indicating faster HGR and increased activity with lower activation energy.[48] The primary reason for that could be attributed to the unique nanosheet structure of the catalyst, which provides a larger active surface area, resulting in an increased gas diffusion rate and facilitating the mass transfer of the catalyst.[49]

The Co_2B-Fe_2B catalyst's reusability in $NaBH_4$ hydrolysis was evaluated by performing five consecutive cycles with the same catalyst. The results depicted in Figure 4e,f show that the HGR decreased to only 84% after five cycles, indicating exceptional stability. To investigate why the Co_2B-Fe_2B catalyst showed remarkable reusability, its morphology, crystal structure, and surface electronic state were examined after stability testing. The catalyst's morphology and crystal structure remained almost unchanged after five cycles (Figures S8 and S9). Additionally, XPS analysis of the stabilized sample revealed the presence of Co, Fe, and B elements in the full spectrum, which was consistent with the prereaction results (Figure S10). Moreover, the high-resolution XPS of Co 2p, Fe 2p, and B 1s exhibited no significant changes even after the repeatability test (Figure S11). These results indicated that the Co_2B-Fe_2B catalyst had a robust surface structure that protected the active centers from damage. The slight decrease in HGR could be attributed to the slight spalling of the catalyst and the poisoning effect of BO_2^-.[50]

DFT Calculations. To investigate the exceptional catalytic activity of the Co_2B-Fe_2B heterostructure, DFT calculations were performed. Previous studies have demonstrated that H_2 generated by $NaBH_4$ hydrolysis is derived equally from H_2O and BH_4^- through a bimolecular reaction (eq 1). The charge-density distribution of the heterogeneous structure in Figure 5a shows significant charge accumulation at the interface, indicating a strong electronic synergistic effect between Co_2B and Fe_2B. Furthermore, BH_4^* and H_2O^* were identified as important descriptors for the hydrolysis reaction catalyzed by $NaBH_4$. BH_4^* exhibited optimal ΔG_{BH4^*} at the Co_2B site (−3.18 eV) compared with Fe_2B (−3.05 eV) (Figure 5b), while H_2O^* displayed the best ΔG_{H2O^*} at the Fe_2B site (−0.53 eV) compared with Co_2B (−0.47 eV) (Figure 5c). Thus, BH_4^- tends to adsorb at the Co_2B site of the Co_2B-Fe_2B heterostructure, while H_2O adsorbs at the Fe_2B site.

The Langmuir−Hinshelwood and Michaelis−Menten mechanisms are the two most widely accepted mechanisms in $NaBH_4$ hydrolysis.[51] DFT calculations revealed that the Michaelis−Menten mechanism was the optimized mechanism for H_2 generation (Figures S12−S14). As shown in Figure 5d, the BH_4^* adsorbed at the Co_2B site was first activated and decomposed to H_{ad}, which was an exothermic reaction step (Table S1). Subsequently, H_{ad} combined with another H_{ad} generated from adsorbed H_2O to release a H_2 molecule. From the decisive step of the transition state (TS), it can be found that Co_2B-Fe_2B (ΔG_4 = 1.18 eV) exhibited the lowest transition state energy barrier compared with those of Co_2B (ΔG_4 = 1.68 eV) and Fe_2B (ΔG_4 = 1.90 eV), which indicated the faster catalytic activity. Then, the adsorbed OH (OH_{ad}) conducted a nucleophilic attack on the adsorbed BH_3 to generate BH_3OH, thus completing the first H_2 generation process of $NaBH_4$ hydrolysis.[52] Simulations of the complete hydrolysis schematic revealed that, as the reaction proceeded, the remaining H atoms in the borohydride were entirely replaced by OH^-, and eventually, the $B(OH)_4^-$ was dissociated to rerelease new active site (Figure 5e).[46] Overall, the exceptional catalytic activity of the Co_2B-Fe_2B catalyst can be attributed to the following factors: (1) the unique nanosheet structure exposed more active sites and enhanced the intrinsic activity of the catalyst; (2) a defect-rich catalyst can effectively modulate the carrier concentration and promote the synergy between components; and (3) strong electronic interactions between the components can reduce the reaction intermediate state energy barrier of the catalyst and increase the catalytic reaction rate.

■ CONCLUSIONS

In conclusion, this study demonstrates the successful synthesis of a highly efficient Co_2B-Fe_2B catalyst for the generation of hydrogen from $NaBH_4$ hydrolysis. The use of a NaCl template and vacancy engineering strategy allowed for the creation of a uniformly dispersed composite with abundant boron vacancies, providing a favorable condition for rapid electron transfer and exposure of active sites. The optimized Co_2B-Fe_2B catalyst displayed superior catalytic performance, with a high HGR value of 5315.8 mL min^{-1} g^{-1} and a low activation energy of 35.4 kJ mol^{-1}, surpassing most published nonprecious metal catalysts. DFT calculations revealed that the Michaelis−Menten mechanism was the optimal reaction pathway for H_2 production, and the low transition state reaction energy barrier of the Co_2B-Fe_2B catalyst further contributed to its excellent catalytic performance. The catalyst also exhibited remarkable stability for $NaBH_4$ hydrolysis, indicating its potential as a practical alternative to noble metal-based catalysts. This work

provides a novel and simplified approach to developing nonnoble metal-based catalysts for NaBH$_4$ hydrolysis with high activity, robustness, and uniform dispersion.

■ ASSOCIATED CONTENT

Ⓢ Supporting Information

The Supporting Information is available free of charge at https://pubs.acs.org/doi/10.1021/acs.inorgchem.3c03746.

Additional experimental details, including catalyst synthesis, methods for material characterization, theoretical calculation, catalytic hydrolysis performance, SEM images, XPS spectra, and XRD patterns (PDF)

■ AUTHOR INFORMATION

Corresponding Authors

Wei Li − Guangxi Key Laboratory of Low Carbon Energy Materials, School of Chemistry and Pharmaceutical Sciences, Guangxi Normal University, Guilin 541004, China; Email: liwei@gxnu.edu.cn

Shoulei Xu − School of Physical Science and Technology, Guangxi University, Nanning 530004, China; Email: xsl@gxu.edu.cn

Xiulin Yang − Guangxi Key Laboratory of Low Carbon Energy Materials, School of Chemistry and Pharmaceutical Sciences, Guangxi Normal University, Guilin 541004, China; ⓞ orcid.org/0000-0003-2642-4963; Email: xlyang@gxnu.edu.cn

Authors

Shuqing Zhou − Guangxi Key Laboratory of Low Carbon Energy Materials, School of Chemistry and Pharmaceutical Sciences, Guangxi Normal University, Guilin 541004, China

Lianrui Cheng − Guangxi Key Laboratory of Low Carbon Energy Materials, School of Chemistry and Pharmaceutical Sciences, Guangxi Normal University, Guilin 541004, China

Yi Liu − Guangxi Key Laboratory of Low Carbon Energy Materials, School of Chemistry and Pharmaceutical Sciences, Guangxi Normal University, Guilin 541004, China

Jianniao Tian − Guangxi Key Laboratory of Low Carbon Energy Materials, School of Chemistry and Pharmaceutical Sciences, Guangxi Normal University, Guilin 541004, China; ⓞ orcid.org/0000-0002-0404-2713

Chenggong Niu − Guangxi Key Laboratory of Low Carbon Energy Materials, School of Chemistry and Pharmaceutical Sciences, Guangxi Normal University, Guilin 541004, China

Tayirjan Taylor Isimjan − Saudi Arabia Basic Industries Corporation (SABIC) at King Abdullah University of Science and Technology (KAUST), Thuwal 23955-6900, Saudi Arabia; ⓞ orcid.org/0000-0003-1735-481X

Complete contact information is available at:
https://pubs.acs.org/10.1021/acs.inorgchem.3c03746

Author Contributions

The manuscript was written through contributions of all authors. All authors have given approval to the final version of the manuscript. S.Z. and L.C. contributed equally to this work.

Notes

The authors declare no competing financial interest.

■ ACKNOWLEDGMENTS

■ REFERENCES

(1) Nguyen, D. C.; Luyen doan, T. L.; Prabhakaran, S.; Tran, D. T.; Kim, D. H.; Lee, J. H.; Kim, N. H. Hierarchical Co and Nb dual-doped MoS$_2$ nanosheets shelled micro-TiO$_2$ hollow spheres as effective multifunctional electrocatalysts for HER, OER, and ORR. Nano Energy **2021**, 82, No. 105750.

(2) Yusuf, B. A.; Yaseen, W.; Xie, M.; Zayyan, R. S.; Muhammad, A. I.; Nankya, R.; Xie, J.; Xu, Y. Recent advances in understanding and design of efficient hydrogen evolution electrocatalysts for water splitting: A comprehensive review. Adv. Colloid Interface Sci. **2023**, 311, No. 102811.

(3) Xiong, J.; Li, J.; Shi, J. W.; Zhang, X. L.; Cai, W. W.; Yang, Z. H.; Cheng, H. S. Metallic 1T-MoS$_2$ nanosheets in-situ entrenched on N,P,S-codoped hierarchical carbon microflower as an efficient and robust electro-catalyst for hydrogen evolution. Appl. Catal. B Environ. **2019**, 243, 614−620.

(4) Yuan, H.; Wang, S.; Ma, Z.; Kundu, M.; Tang, B.; Li, J.; Wang, X. Oxygen vacancies engineered self-supported B doped Co$_3$O$_4$ nanowires as an efficient multifunctional catalyst for electrochemical water splitting and hydrolysis of sodium borohydride. Chem. Eng. J. **2021**, 404, No. 126474.

(5) Zhang, J.; Lin, F.; Yang, L.; He, Z.; Huang, X.; Zhang, D.; Dong, H. Ultrasmall Ru nanoparticles supported on chitin nanofibers for hydrogen production from NaBH$_4$ hydrolysis. Chin. Chem. Lett. **2020**, 31, 2019−2022.

(6) Hou, Q.; Wu, Y.; Zhou, S.; Wei, Y.; Caro, J.; Wang, H. Ultra-Tuning of the Aperture Size in Stiffened ZIF-8_Cm Frameworks with Mixed-Linker Strategy for Enhanced CO$_2$/CH$_4$ Separation. Angew. Chem., Int. Ed. **2019**, 58, 327−331.

(7) Peng, D.; Zhang, Y.; Han, S. Fabrication of Multiple-Phase Magnesium-Based Hydrides with Enhanced Hydrogen Storage Properties by Activating NiS@C and Mg Powder. ACS Sustain. Chem. Eng. **2021**, 9, 998−1007.

(8) Liu, X.; Mcgrady, G. S.; Langmi, H. W.; Jensen, C. M. Facile cycling of Ti-doped LiAlH$_4$ for high performance hydrogen storage. J. Am. Chem. Soc. **2009**, 131, 5032−3.

(9) Usman, M. R. Hydrogen storage methods: Review and current status. Renew. Sust. Energy Rev. **2022**, 167, No. 112743.

(10) Zhang, J.; Lin, F.; Yang, L.; Dong, H. Highly dispersed Ru/Co catalyst with enhanced activity for catalyzing NaBH$_4$ hydrolysis in alkaline solutions. Chin. Chem. Lett. **2020**, 31, 2512−2515.

(11) Zhong, H.; Ouyang, L.; Zeng, M.; Liu, J.; Wang, H.; Shao, H.; Felderhoff, M.; Zhu, M. Realizing facile regeneration of spent NaBH$_4$ with Mg−Al alloy. J. Mater. Chem. A **2019**, 7, 10723−10728.

(12) Zhu, Y.; Ouyang, L.; Zhong, H.; Liu, J.; Wang, H.; Shao, H.; Huang, Z.; Zhu, M. Closing the Loop for Hydrogen Storage: Facile Regeneration of NaBH$_4$ from its Hydrolytic Product. Angew. Chem., Int. Ed. **2020**, 59, 8623−8629.

(13) Dou, S.; Zhou, S.; Huang, H.; Yan, P.; Shoko, E.; Isimjan, T. T.; Yang, X. Metal-Organic Framework (MOF)-Derived Electron-Transfer Enhanced Homogeneous PdO-Rich Co$_3$O$_4$ as a Highly Efficient Bifunctional Catalyst for Sodium Borohydride Hydrolysis and 4-Nitrophenol Reduction. Chem.—Eur. J. **2020**, 26, 16923−16931.

(14) Fernandes, R.; Patel, N.; Miotello, A. Hydrogen generation by hydrolysis of alkaline NaBH$_4$ solution with Cr-promoted Co−B amorphous catalyst. Appl. Catal. B Environ. **2009**, 92, 68−74.

(15) Saka, C.; Kaya, M.; Bekiroğullari, M. Spirulina Platensis microalgae strain modified with phosphoric acid as a novel support material for Co−B catalysts: Its application to hydrogen production. Int. J. Hydrogen Energy **2020**, 45, 2872−2883.

(16) Paksoy, A.; Kurtoğlu, S. F.; Dizaji, A. K.; Altıntaş, Z.; Khoshsima, S.; Uzun, A.; Balcı, Ö. Nanocrystalline cobalt−nickel−boron (metal boride) catalysts for efficient hydrogen production from the hydrolysis of sodium borohydride. *Int. J. Hydrogen Energy* **2021**, *46*, 7974−7988.

(17) Guo, J.; Wu, C.; Zhang, J.; Yan, P.; Tian, J.; Shen, X.; Isimjan, T. T.; Yang, X. Hierarchically structured rugae-like RuP₃−CoP arrays as robust catalysts synergistically promoting hydrogen generation. *J. Mater. Chem. A* **2019**, *7*, 8865−8872.

(18) Wang, W.; Chen, W.; Miao, P.; Luo, J.; Wei, Z.; Chen, S. NaCl Crystallites as Dual-Functional and Water-Removable Templates To Synthesize a Three-Dimensional Graphene-like Macroporous Fe-N-C Catalyst. *ACS Catal.* **2017**, *7*, 6144−6149.

(19) Zeng, H.; Wang, W.; Li, J.; Luo, J.; Chen, S. In Situ Generated Dual-Template Method for Fe/N/S Co-Doped Hierarchically Porous Honeycomb Carbon for High-Performance Oxygen Reduction. *ACS Appl. Mater. Interfaces* **2018**, *10*, 8721−8729.

(20) Xiong, J.; Di, J.; Xia, J.; Zhu, W.; Li, H. Surface Defect Engineering in 2D Nanomaterials for Photocatalysis. *Adv. Funct. Mater.* **2018**, *28*, No. 1801983.

(21) Shi, L.; Zhu, K.; Yang, Y.; Liu, Y.; Xu, S.; Isimjan, T. T.; Yang, X. Oxygen-vacancy-rich Ru-clusters decorated Co/Ce oxides modifying ZIF-67 nanocubes as a high-efficient catalyst for NaBH₄ hydrolysis. *Int. J. Hydrogen Energy* **2022**, *47*, 37840−37849.

(22) Zhou, S.; Yang, Y.; Zhang, W.; Rao, X.; Yan, P.; Isimjan, T. T.; Yang, X. Structure-regulated Ru particles decorated P-vacancy-rich CoP as a highly active and durable catalyst for NaBH₄ hydrolysis. *J. Colloid Interface Sci.* **2021**, *591*, 221−228.

(23) Masa, J.; Weide, P.; Peeters, D.; Sinev, I.; Xia, W.; Sun, Z.; Somsen, C.; Muhler, M.; Schuhmann, W. Amorphous Cobalt Boride (Co₂B) as a Highly Efficient Nonprecious Catalyst for Electrochemical Water Splitting: Oxygen and Hydrogen Evolution. *Adv. Energy Mater.* **2016**, *6*, No. 1502313.

(24) Jiang, R.; Shi, Z.; Zhao, W.; Gao, B.; Wu, T.; Yuan, Q. Vacancy-Assisted Growth Mechanism of Multilayer Hexagonal Boron Nitride on a Fe₂B Substrate. *J. Phys. Chem. Lett.* **2020**, *11*, 8511−8517.

(25) Han, H.; Choi, H.; Mhin, S.; Hong, Y.-R.; Kim, K. M.; Kwon, J.; Ali, G.; Chung, K. Y.; Je, M.; Umh, H. N.; Lim, D.-H.; Davey, K.; Qiao, S.-Z.; Paik, U.; Song, T. Advantageous crystalline−amorphous phase boundary for enhanced electrochemical water oxidation. *Energy Environ. Sci.* **2019**, *12*, 2443−2454.

(26) Guo, Y.; Yao, Z.; Shang, C.; Wang, E. Amorphous Co₂B Grown on CoSe₂ Nanosheets as a Hybrid Catalyst for Efficient Overall Water Splitting in Alkaline Medium. *ACS Appl. Mater. Interfacess* **2017**, *9*, 39312−39317.

(27) Jian, Y.; Huang, Z.; Liu, X.; Sun, J.; Xing, J. Microstructure, mechanical properties and toughening mechanism of directional Fe₂B crystal in Fe-B alloy with trace Cr addition. *J. Mater. Sci. Technol.* **2020**, *57*, 172−179.

(28) Wu, P.; Jia, Q.; He, J.; Lu, L.; Chen, L.; Zhu, J.; Peng, C.; He, M.; Xiong, J.; Zhu, W.; Li, H. Mechanical exfoliation of boron carbide: A metal-free catalyst for aerobic oxidative desulfurization in fuel. *J. Hazard. Mater.* **2020**, *391*, No. 122183.

(29) Chao, Y.; Tang, B.; Luo, J.; Wu, P.; Tao, D.; Chang, H.; Chu, X.; Huang, Y.; Li, H.; Zhu, W. Hierarchical porous boron nitride with boron vacancies for improved adsorption performance to antibiotics. *J. Colloid Interface Sci.* **2021**, *584*, 154−163.

(30) Gottscholl, A.; Kianinia, M.; Soltamov, V.; Orlinskii, S.; Mamin, G.; Bradac, C.; Kasper, C.; Krambrock, K.; Sperlich, A.; Toth, M.; Aharonovich, I.; Dyakonov, V. Initialization and read-out of intrinsic spin defects in a van der Waals crystal at room temperature. *Nat. Mater.* **2020**, *19*, 540−545.

(31) Gao, X.; Pandey, S.; Kianinia, M.; Ahn, J.; Ju, P.; Aharonovich, I.; Shivaram, N.; Li, T. Femtosecond Laser Writing of Spin Defects in Hexagonal Boron Nitride. *ACS Photonics* **2021**, *8*, 994−1000.

(32) Sathiya, M.; Leriche, J. B.; Salager, E.; Gourier, D.; Tarascon, J. M.; Vezin, H. Electron paramagnetic resonance imaging for real-time monitoring of Li-ion batteries. *Nat. Commun.* **2015**, *6*, 6276.

(33) Li, Y.; Chu, F.; Bu, Y.; Kong, Y.; Tao, Y.; Zhou, X.; Yu, H.; Yu, J.; Tang, L.; Qin, Y. Controllable fabrication of uniform ruthenium phosphide nanocrystals for the hydrogen evolution reaction. *Chem. Commun.* **2019**, *55*, 7828−7831.

(34) Santra, S.; Das, D.; Das, N. S.; Nanda, K. K. An efficient on-board metal-free nanocatalyst for controlled room temperature hydrogen production. *Chem. Sci.* **2017**, *8*, 2994−3001.

(35) Lu, Y.; Li, C.; Zhang, Y.; Cao, X.; Xie, G.; Wang, M.; Peng, D.; Huang, K.; Zhang, B.; Wang, T.; Junsheng, W.; Huang, Y. Engineering of cation and anion vacancies in Co₃O₄ thin nanosheets by laser irradiation for more advancement of oxygen evolution reaction. *Nano Energy* **2021**, *83*, No. 105800.

(36) Zhou, S.; Cheng, L.; Huang, Y.; Liu, Y.; Shi, L.; Isimjan, T. T.; Yang, X. Constructing Ru particles decorated Co₃B-CoP heterostructures as a highly active and reusable catalyst for H₂ generation by catalyzing NaBH₄ hydrolysis. *Appl. Catal. B Environ.* **2023**, *328*, No. 122519.

(37) Masa, J.; Sinev, I.; Mistry, H.; Ventosa, E.; De la mata, M.; Arbiol, J.; Muhler, M.; Roldan cuenya, B.; Schuhmann, W. Ultrathin High Surface Area Nickel Boride (NiₓB) Nanosheets as Highly Efficient Electrocatalyst for Oxygen Evolution. *Adv. Energy Mater.* **2017**, *7*, No. 1700381.

(38) Jiang, B.; Song, H.; Kang, Y.; Wang, S.; Wang, Q.; Zhou, X.; Kani, K.; Guo, Y.; Ye, J.; Li, H.; Sakka, Y.; Henzie, J.; Yusuke, Y. A mesoporous non-precious metal boride system: synthesis of mesoporous cobalt boride by strictly controlled chemical reduction. *Chem. Sci.* **2020**, *11*, 791−796.

(39) Liu, Q.; Zhao, H.; Jiang, M.; Kang, Q.; Zhou, W.; Wang, P.; Zhou, F. Boron enhances oxygen evolution reaction activity over Ni foam-supported iron boride nanowires. *J. Mater. Chem. A* **2020**, *8*, 13638−13645.

(40) Zhang, Q.; Liang, S.-X.; Jia, Z.; Zhang, W.; Wang, W.; Zhang, L.-C. Efficient nanostructured heterogeneous catalysts by electrochemical etching of partially crystallized Fe-based metallic glass ribbons. *J. Mater. Sci. Technol.* **2021**, *61*, 159−168.

(41) Ma, X.; Wen, J.; Zhang, S.; Yuan, H.; Li, K.; Yan, F.; Zhang, X.; Chen, Y. Crystal CoₓB (x = 1−3) Synthesized by a Ball-Milling Method as High-Performance Electrocatalysts for the Oxygen Evolution Reaction. *ACS Sustain. Chem. Eng.* **2017**, *5*, 10266−10274.

(42) Gnanamani, M. K.; Jacobs, G.; Hamdeh, H. H.; Shafer, W. D.; Liu, F.; Hopps, S. D.; Thomas, G. A.; Davis, B. H. Hydrogenation of Carbon Dioxide over Co−Fe Bimetallic Catalysts. *ACS Catal.* **2016**, *6*, 913−927.

(43) Zhang, P.; Lu, X. F.; Nai, J.; Zang, S. Q.; Lou, X. W. D. Construction of Hierarchical Co-Fe Oxyphosphide Microtubes for Electrocatalytic Overall Water Splitting. *Adv. Sci.* **2019**, *6*, No. 1900576.

(44) Saka, C. Highly active and durable hydrogen release in NaBH₄ methanolysis reaction with sulphur and phosphorus-doped metal-free microalgal carbon nanoparticles. *Appl. Catal. B Environ.* **2021**, *292*, No. 120165.

(45) Cao, X.; Zhou, J.; Zhai, Z.; Li, S.; Yuan, G.; Qin, G. Synchronous Growth of Porous MgO and Half-Embedded Nano-Ru on a Mg Plate: A Monolithic Catalyst for Fast Hydrogen Production. *ACS Sustain. Chem. Eng.* **2021**, *9*, 3616−3623.

(46) Zhang, H.; Zhang, L.; Rodríguez-pérez, I. A.; Miao, W.; Chen, K.; Wang, W.; Li, Y.; Han, S. Carbon nanospheres supported bimetallic Pt-Co as an efficient catalyst for NaBH₄ hydrolysis. *Appl. Surf. Sci.* **2021**, *540*, No. 148296.

(47) Tuan, D. D.; Lin, K.-Y. A. Ruthenium supported on ZIF-67 as an enhanced catalyst for hydrogen generation from hydrolysis of sodium borohydride. *Chem. Eng. J.* **2018**, *351*, 48−55.

(48) Deonikar, V. G.; Rathod, P. V.; Pornea, A. M.; Puguan, J. M. C.; Park, K.; Kim, H. Hydrogen generation from catalytic hydrolysis of sodium borohydride by a Cu and Mo promoted Co catalyst. *J. Ind. Eng. Chem.* **2020**, *86*, 167−177.

(49) Guo, J.; Hou, Y.; Li, B.; Liu, Y. Novel Ni−Co−B hollow nanospheres promote hydrogen generation from the hydrolysis of sodium borohydride. *Int. J. Hydrog. Energy* **2018**, *43*, 15245−15254.

(50) Zhou, L. M.; Meng, J.; Li, P.; Tao, Z. L.; Mai, L. Q.; Chen, J. Ultrasmall cobalt nanoparticles supported on nitrogen-doped porous carbon nanowires for hydrogen evolution from ammonia borane. *Mater. Horizons* **2017**, *4*, 268−273.

(51) Demirci, U. B.; Miele, P. Reaction mechanisms of the hydrolysis of sodium borohydride: A discussion focusing on cobalt-based catalysts. *C. R. Chimie* **2014**, *17*, 707−716.

(52) Kassem, A. A.; Abdelhamid, H. N.; Fouad, D. M.; Ibrahim, S. A. Metal-organic frameworks (MOFs) and MOFs-derived CuO@C for hydrogen generation from sodium borohydride. *Int. J. Hydrogen Energy* **2019**, *44*, 31230−31238.